ADVANCING EARTH AND SPACE SCIENCE

Geophysical Research Letters

RESEARCH LETTER
10.1029/2022GL100306

Key Points:

- Three ground and space missions observed the formation and evolution of plasmaspheric plume following a strong substorm
- Hiss waves propagating oppositely in the nightside plasmaspheric plume and core correlated highly with each other at a time lag of 4–10 s
- Numerical modeling supports that the plasmaspheric plume allows hiss waves to grow and then migrate to the plasmaspheric core

Supporting Information:

Supporting Information may be found in the online version of this article.

Correspondence to:

Z. Su and Z. He,
szpe@mail.ustc.edu.cn;
hezhg3@mail.sysu.edu.cn

Citation:

Wu, Z., Su, Z., Goldstein, J., Liu, N., He, Z., Zheng, H., & Wang, Y. (2022). Nightside plasmaspheric plume-to-core migration of whistler-mode hiss waves. *Geophysical Research Letters*, *49*, e2022GL100306. https://doi.org/10.1029/2022GL100306

Received 4 JUL 2022
Accepted 14 AUG 2022

Nightside Plasmaspheric Plume-To-Core Migration of Whistler-Mode Hiss Waves

Zhiyong Wu[1,2,3], Zhenpeng Su[1,2], Jerry Goldstein[4,5], Nigang Liu[6], Zhaoguo He[6], Huinan Zheng[1,2], and Yuming Wang[1,2]

[1]CAS Key Laboratory of Geospace Environment, Department of Geophysics and Planetary Sciences, University of Science and Technology of China, Hefei, China, [2]CAS Center for Excellence in Comparative Planetology, University of Science and Technology of China, Hefei, China, [3]Anhui Mengcheng Geophysics National Observation and Research Station, University of Science and Technology of China, Mengcheng, China, [4]Space Science and Engineering Division, Southwest Research Institute, San Antonio, TX, USA, [5]Department of Physics and Astronomy, University of Texas at San Antonio, San Antonio, TX, USA, [6]School of Atmospheric Science, Sun Yat-sen University, Zhuhai, China

Abstract Whistler-mode hiss waves play an important role in the radiation belt electron depletion. Whether the hiss waves with significant differences in amplitude and propagation direction within the plasmaspheric core and plume are related to each other remains unclear. We here show that the plasmaspheric plume facilitates the energy conversion from energetic electrons to hiss waves and then guides hiss waves into the plasmaspheric core. Three ground and space missions captured the initial formation and subsequent rotation of the plasmaspheric plume in the noon-dusk-midnight sector following a strong substorm. The observed hiss waves in the nightside plasmaspheric plume and core propagated oppositely but highly correlated with each other at a time lag of 4–10 s. The linear instability of energetic electrons in the plasmaspheric plume qualitatively explains the frequency-dependence of hiss waves, and the ray-tracing modeling reproduces the propagation direction and timing of hiss waves.

Plain Language Summary In the Earth's inner magnetosphere, plasmaspheric hiss is a natural band of whistler-mode waves spanning from tens of hertz to several kilohertz. It was so named because it is confined to the dense plasmasphere and sounds like white noise when played through a loudspeaker. It is well known that both the plasmaspheric core and plume sustain hiss waves and these waves differ significantly in both amplitude and propagation direction. However, whether these hiss waves of different regions are related or not remains unclear. On the basis of data from three ground and space missions and detailed modeling, we show that the plasmaspheric plume facilitates the energy conversion from energetic electrons to hiss waves and then guides hiss waves into the plasmaspheric core. This depiction of the plume's role could be generalized toward other plasmaspheric structures extending outward such as the plasmaspheric bulge, fingers, and crenulations.

1. Introduction

The Earth's plasmasphere arises from the sunlit-driven outflow of ionized particles of the upper atmosphere along the magnetic field at low and middle latitudes (Borovsky & Valdivia, 2018; Darrouzet et al., 2009; Foster et al., 2002; Lemaire & Gringauz, 1998). During quiet times, the plasmasphere persists as a torus of cold, dense plasma circling the Earth. During disturbed times, the outer plasmaspheric plasma are drained toward the dayside magnetopause to form a plume that survives with an evolving shape for tens of hours (Goldstein et al., 2004). The plasmaspheric core (main body of the plasmasphere) and plume sustain the whistler-mode hiss waves from tens of hertz to several kilohertz (Dunckel & Helliwell, 1969; Li et al., 2013; Russell et al., 1969; Summers et al., 2008; Thorne et al., 1973; Tsurutani et al., 1975), which contribute to the depletion of the radiation belt electrons through cyclotron resonance (Breneman et al., 2015; Horne & Thorne, 1998; Li et al., 2007; Lyons et al., 1972; Meredith et al., 2007; Ni et al., 2014; Su et al., 2011; Summers et al., 1998; Thorne et al., 2013).

There have been two competing classes of hiss generation mechanisms proposed since the 1970s (Bortnik, Thorne, & Meredith, 2009). One envisions that energetic electrons directly amplify thermal noises into hiss waves just inside the plasmapause and further spread within the entire plasmasphere (He et al., 2019, 2020; Li et al., 2013; Liu et al., 2020; Thorne et al., 1973). In the framework of linear instability of energetic electrons, hiss waves experience the cyclic amplification in the outer plasmaspheric core (Chen et al., 2014; Thorne et al., 1973, 1979). Inspired by observations (Summers et al., 2014) that a seemingly noisy hiss wave band was composed of coherent rising and falling tone elements of 10–100 ms, Omura et al. (2015) proposed the nonlinear growth of hiss waves. The nonlinear growth rate of hiss waves is much larger than the linear one (Nakamura et al., 2016; Omura et al., 2015). Su et al. (2018a, 2018b) and Liu et al. (2020) suggested the local generation of hiss waves of tens of Hz to several kHz through a combination of linear and nonlinear instabilities of energetic electrons in the plasmaspheric plume and core on both dayside and nightside. The other envisions that lightening-generated whistler-mode waves in the atmosphere (Green et al., 2005; Sonwalkar & Inan, 1989) and whistler-mode chorus waves outside the plasmasphere (Bortnik et al., 2008; Bortnik, Li, et al., 2009; Chen, Bortnik, et al., 2012; Chen, Li, et al., 2012; Li et al., 2015; Meredith et al., 2013; Wang et al., 2011) can enter the plasmasphere and be further amplified by energetic electrons into hiss waves (Church & Thorne, 1983). There is no consensus on the relative importance of internal excitation and external origination mechanisms, although several proposals such as dependence on the magnetic local time (MLT) (Tsurutani et al., 2015) and the wave frequency (Meredith et al., 2021) exist.

Compared to the plasmaspheric core, the plasmaspheric plume usually sustains stronger hiss waves (Chan et al., 1974; Nakamura et al., 2018; Su et al., 2018a; Summers et al., 2008; Zhang et al., 2019). In contrast to the hiss waves typically with unordered Poynting fluxes in the plasmaspheric core, the plasmaspheric plume hiss waves usually propagate quasi-parallel away from the magnetic equator (Hayakawa et al., 1986; Kim & Shprits, 2019; Laakso et al., 2015; Nakamura et al., 2018; Shi et al., 2019; Su et al., 2018a; Yu et al., 2018). Whether the hiss waves inside the plasmaspheric core and plume are related to each other remains unclear. On the basis of observations of hiss wave Poynting fluxes in the plasmaspheric plume and core, Laakso et al. (2015) speculated that the hiss waves inside the plasmaspheric core originate from the equatorial region of the plasmaspheric plume. However, experimentally assessing this hypothesis is challenging because of the technical difficulty in identifying the complex, time-varying morphological structures of the plasmasphere from in-situ measurements and the rigorous requirement of simultaneously observing waves inside both the plasmaspheric plume and the plasmaspheric core along the same propagation path. In this letter, we present complete observations from the global positioning system (GPS), the Time History of Events and Macroscale Interactions during Substorms (THEMIS) mission (Angelopoulos, 2008) and the Van Allen Probes (formerly known as the Radiation Belt Storm Probes (RBSP)) mission (Mauk et al., 2013) of the dynamic evolution of the plasmaspheric morphology, the generation of hiss waves inside the plasmaspheric plume, and the propagation of hiss waves into the plasmaspheric core. Furthermore, our modeling results reasonably explain the frequency-dependence and propagation direction and timing of hiss waves in the plasmaspheric core and plume.

2. Identification of Plasmaspheric Structures and Waves

We use the total electron content (TEC) maps of the GPS mission to identify the strong plasmaspheric plume emerged initially on the dayside (Foster et al., 2004; Goldstein et al., 2004). The GPS mission consists of a ground station network and a satellite constellation in circular orbits of an altitude of approximately 20,200 km. The phase delays of radio signals sent by satellites to ground stations allow the total content of free electrons in the upper atmosphere to be inferred. The original TEC maps possess a temporal resolution of 15 min and a spatial resolution of 2.5° latitude and 5.0° longitude in the geographical coordinate system. We project the TEC measurements to the equatorial plane of the geocentric solar magnetic coordinate system along the magnetic field lines of the combined International Geomagnetic Reference Field (IGRF) (Alken et al., 2021) and TS04 (Tsyganenko & Sitnov, 2005) model.

We use the THEMIS and RBSP missions to locally measure waves and particles in the plasmaspheric core and plume. Both the THEMIS and RBSP missions orbit around Earth's equatorial region. Three satellites of the THEMIS mission, TH-A, TH-D, and TH-E have perigee altitudes of ∼470 km and apogee altitudes of ∼87,330 km. The twin satellites composing the RBSP mission, RBSP-A and RBSP-B, have perigee altitudes of ∼600 km and apogee altitudes of ∼38,000 km. The three-axis electric field instrument (EFI) (Bonnell et al., 2008) and the electrostatic analyzer (ESA) (McFadden et al., 2008) of the THEMIS mission and the electric field and wave (EFW) instrument (Wygant et al., 2013) of the RBSP mission measured the satellite potential as a high-resolution proxy of the cold electron density. A less negative electric potential corresponds to a higher electron density. The high frequency receiver (HFR) of the Electric and Magnetic Field Instrument and Integrated Science (EMFISIS) suite (Kletzing et al., 2013) of the RBSP mission measured the wave electric spectra in the frequency range of ∼10 to ∼500 kHz, from which we can identify the upper hybrid resonance frequency band and then determine the cold electron density following the previously proposed procedure (Kurth et al., 2014). Understanding these density structures measured in-situ requires the global contextual information provided by the plasmapause test particle (PTP) model (Goldstein et al., 2014). The tri-axial fluxgate magnetometer (MAG) of the EMFISIS suite onboard the RBSP mission measured the background magnetic field. The Waveform Receiver of the EMFISIS suite and the EFW instrument onboard the RBSP mission provided the wave electromagnetic spectral matrix in the frequency range from ~3 Hz to ~10 kHz. Using the techniques proposed by early studies (Santolík et al., 2002, 2003, 2010), we determine the wave normal angles and Poynting fluxes from onboard spectral matrix. The Helium Oxygen Proton Electron (HOPE) instrument (Funsten et al., 2013) of the Energetic particle, Composition and the Thermal plasma (ECT) suite (Spence et al., 2013), and the Radiation Belt Storm Probes Ion Composition Experiment (RBSPICE) onboard the RBSP mission measured the electron fluxes in the energy ranges from 1 eV to 54 keV and from 25 keV to 1 MeV.

From 12 to 13 February 2015, the plasmasphere was disturbed mainly by a strong, prolonged substorm (Figure 1a). At approximately 16:00 UT on 12 February, the newly formed plasmaspheric plume was detected by the GPS mission. The enhancement of the TEC at latitudes ≥60° (Figure 1b) signified the presence of the plasmaspheric plume (Figure 1c) projected to the upper atmosphere (Foster et al., 2002). As predicted by the PTP simulation run for this event (Movie S1), in the following tens of hours, the plume narrowed with the ongoing loss of plasma through the magnetopause and wrapped itself around the core with the rotation of Earth (Figures 1g–1j). Previous observations indicated that as plumes narrow with time, their density decreases (Borovsky & Denton, 2008; Goldstein et al., 2004). Presumably because of this density decrease, the weakened plume became undetectable to the GPS mission with limited sensitivity. Fortunately, on 13 February, the THEMIS and the RBSP missions traversed the residual plume, which was characterized as a region with large density fluctuations (Borovsky & Denton, 2008; Nishimura et al., 2022).

In the three-dimensional space, the plasmaspheric core and plume were connected to each other. We differentiate the plasmaspheric plume from the plasmaspheric core in two steps: (a) preliminarily determine the relative timing for the satellite entry into the different plasmaspheric structures predicted by the PTP simulation (Movie S1); (b) visually identify the fluctuating high-density region as the plume and the smooth high-density region as the core. During 12:00–15:00 UT, TH-A, TH-E, and TH-D successively crossed the far end of the residual plume on the duskside (with the magnetic local time MLT ≈ 18–19 hr) at altitudes of approximately 50,000 km (Figures 1d–1f). TH-A probably happened to avoid the channel between the plume and the core and went through the base of the plume into the core. The subsequent plasmaspheric rotation allowed TH-E and TH-D to sample the low-density channel. The boundary of the plasmaspheric core sampled by TH-D around 17:25 UT was sharper than that by TH-E around 16:15 UT, perhaps reflecting the temporal evolution or azimuthal asymmetry of the plasmasphere. During 14:00–18:00 UT, RBSP-A and RBSP-B sampled the base of the residual plume near the midnight (MLT ≈ 0–1 hr) at altitudes of approximately 30,000 km (Figures 2a–2c and 2h). Because of the temporal evolution of the plasmasphere, the twin RBSP satellites in nearly identical orbits detected highly different density profiles. RBSP-B moved from the smooth core through the plume's base to the rotating, lumpy plume during 13:00–18:10 UT, crossed the channel during 18:10–18:50 UT, and reentered the core after 18:50 UT; in contrast, RBSP-A successively crossed the high-density core and plume and the low-density trough before 15:50 UT, passed through the lumpy plume during 15:50–16:45 UT, and through the plume's base reentered the smooth core after 16:45 UT.

During 17:40–17:50 UT, RBSP-B and RBSP-A were inside the midnight plasmaspheric plume and core, respectively. The observed energetic (tens of keV) electron fluxes in the plasmaspheric plume were approximately one order of magnitude higher than those in the plasmaspheric core (Figures 2d and 2i). Meanwhile, the hiss waves of these two regions had similar spectral behaviors from about 100 to 500 Hz but opposite propagation directions. In the lumpy plasmaspheric plume (RBSP-B), the hiss waves propagating at normal angles of 120°–180° toward the South Pole were modulated by the local cold electron density (Figures 2e–2g). In the smooth plasmaspheric core (RBSP-A), the hiss waves exhibited a similar modulation feature, although they propagated toward the equator at normal angles of 0°–60° (Figures 2j–2l). From the plume to the core, the hiss intensity decreased by approximately one order of magnitude. To infer the potential lag correlation between hiss signals in the plasmaspheric plume and core, we calculate the cross-correlation coefficients between them during 17:40 UT and 17:50 UT (Figure 3). There are totally 100 samples in signals during this period. RBSP-A started measuring 4.85 s later than RBSP-B, and both satellites made measurements at a cadence of 6 s. Through the entire frequency band, when the

10.1029/2022GL100306

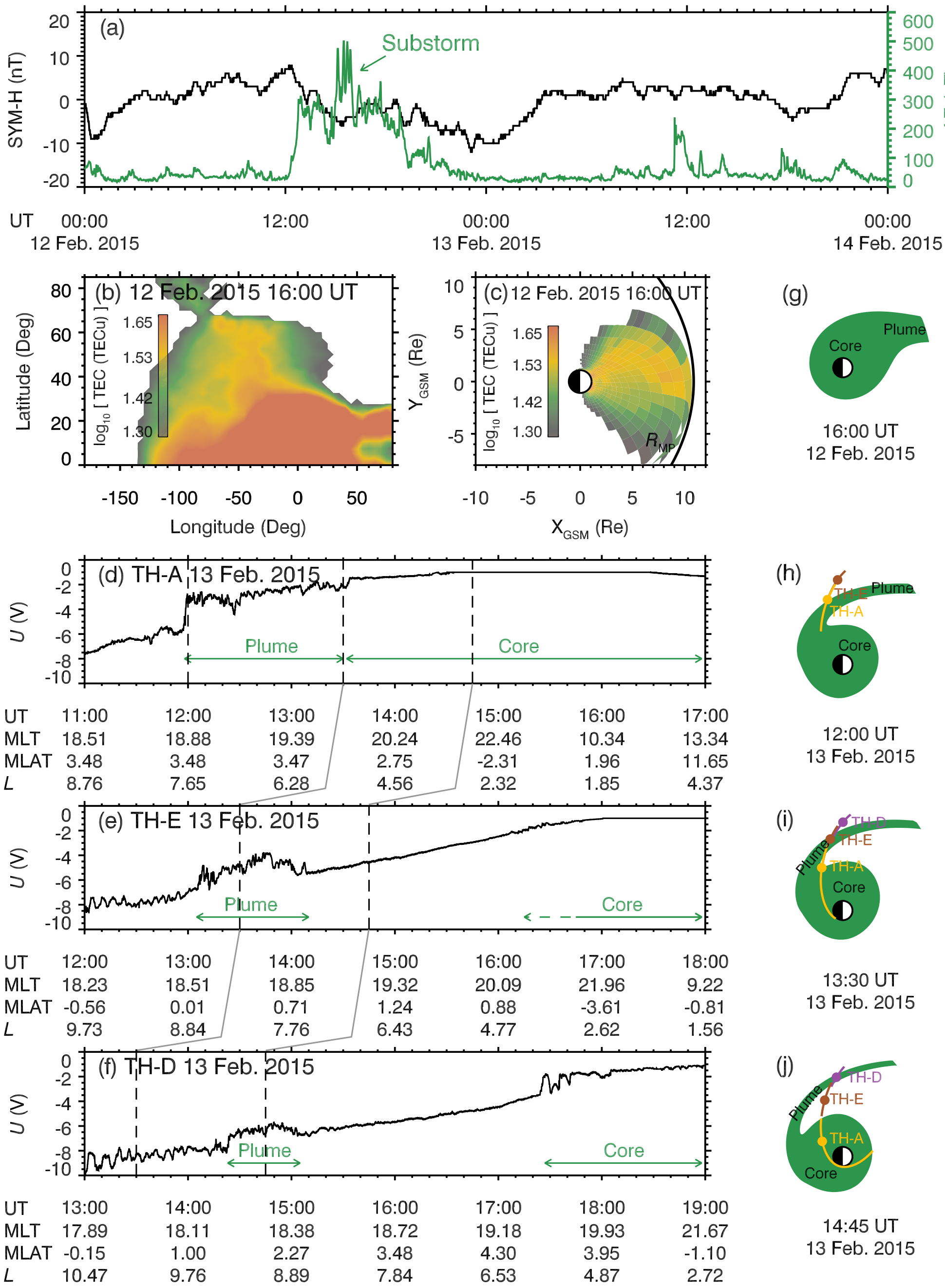

Figure 1. Plasmaspheric structures monitored by the global positioning system (GPS) and Time History of Events and Macroscale Interactions during Substorms (THEMIS) missions from 12 to 13 February 2015. (a) Geomagnetic indices SYM-H (black) and AE (green). (b and c) total electron content (TEC) maps of the GPS mission in the longitude-latitude plane of the geographic coordinate system and in the equatorial plane of the geocentric solar magnetospheric coordinate system overlain by the modeled magnetopause (the black line). (d–f) Electric potentials of three satellites of the THEMIS mission. (g–j) Speculated plasmaspheric structures (green shadows) at four different moments. The plasmaspheric outlines predicted by the plasmapause test particle model have been adjusted artificially to match better the in situ measurements at the specific moments. The lines represent the orbits of the three THEMIS satellites, and the dots mark the locations of the satellites at specific moments. The colors of the lines and dots help differentiate the satellites. The vertical dashed lines in Figures 1d–1f denote the time stamps of Figures 1h–1j.

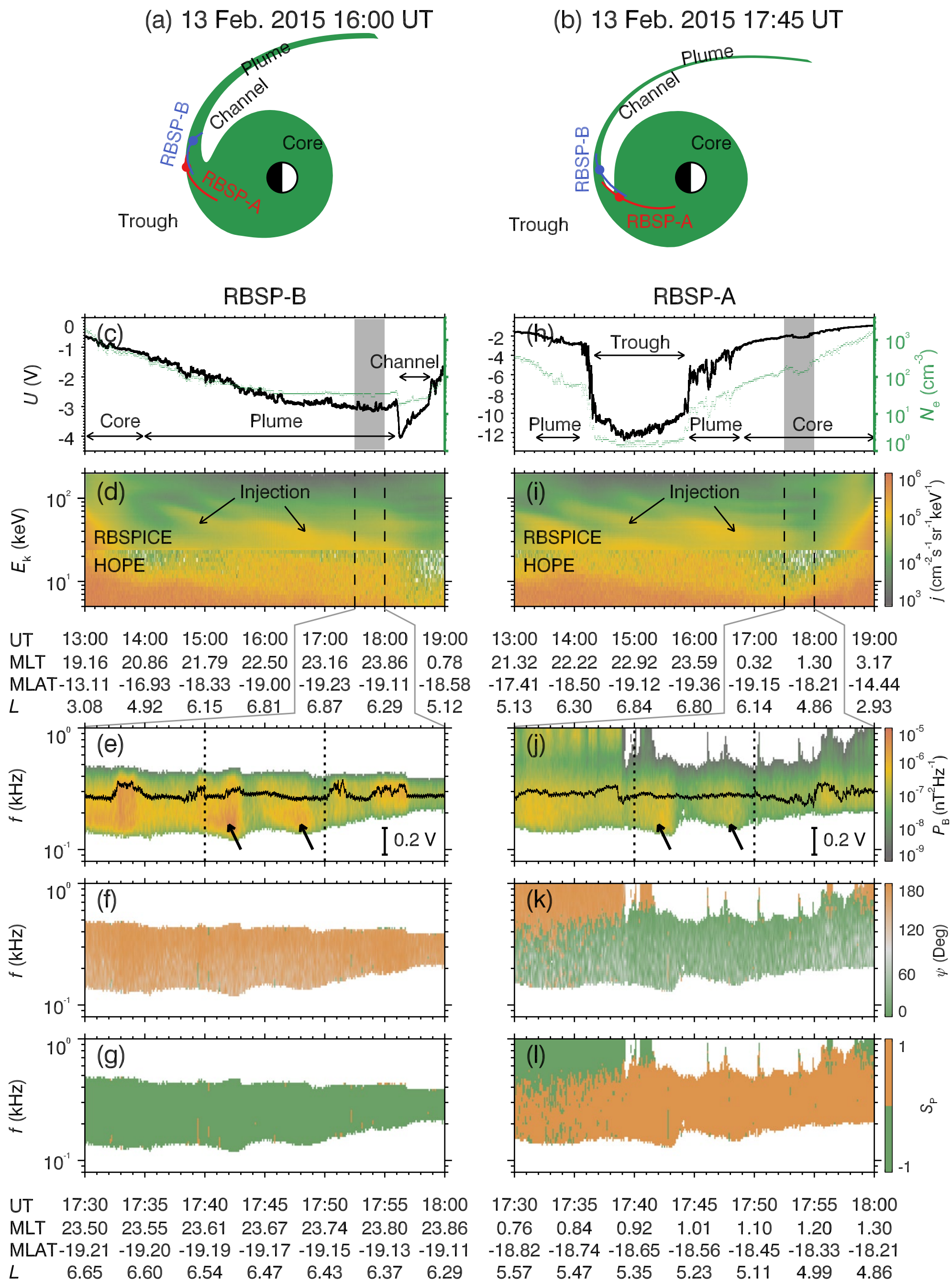

Figure 2. Plasmaspheric structures and waves monitored by the Radiation Belt Storm Probes (RBSP) mission on 13 February 2015. (a and b) Speculated plasmaspheric structures at two different moments in the same format as Figures 1g–1j, except that the orbits and locations of the twin RBSP satellites are overlain. (c and h) Electric potentials and electron densities from 13:00 UT to 19:00 UT. The gray shadow marks the period from 17:30 to 18:00 UT for the magnified plots (e–g and j–l) of the wave characteristics. (d and i) Omnidirectional electron differential flux. (e and j) Wave magnetic power spectral densities. The black lines represent the fluctuations of electric potentials relative to their 10 min running averaged values, with the plotted bar indicating the scale. The vertical dotted lines mark the period during which the twin RBSP satellites observed hiss waves with similar spectral behaviors. The arrows indicate two prominent enhancements of the hiss to facilitate the intercomparison between the twin RBSP satellites. (f and k) Wave normal angles. (g and l) Signs of wave Poynting flux components along the magnetic fields. In Southern Hemisphere, positive values (orange) indicate the propagation of waves toward the equator, and negative values (green) indicate the propagation of waves toward the South Pole.

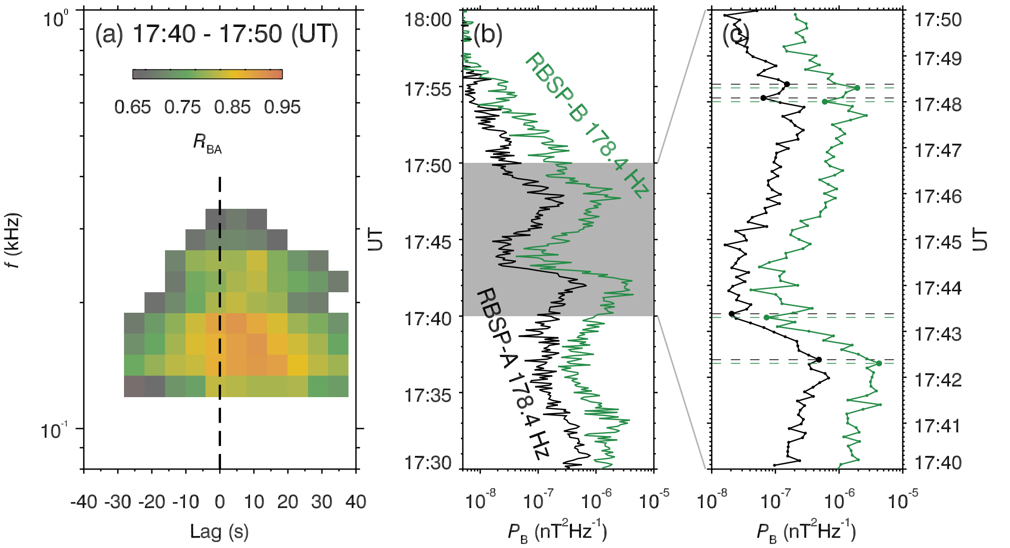

Figure 3. Cross-correlation analysis between waves from RBSP-A and RBSP-B. (a) Cross-correlation coefficients of the common logarithms of magnetic power spectral density data series from RBSP-B and RBSP-A as a function of the wave frequency and time lag. Positive (negative) time lag values represent the lagging (leading) of RBSP-A data with respect to RBSP-B data. (b) Data series of magnetic power spectral densities at 178.4 Hz from RBSP-B (green) and RBSP-A (black) during 17:30–18:00 UT. The gray shadow marks the time range from 17:40 UT to 17:50 UT for the cross-correlation evaluation. (c) Magnified view of the data series, with 100 samples (dots) for each satellite. Four pairs of dots of larger sizes and horizontal dashed lines help identify the lagging correlation between the data of the twin satellites.

core signals lag behind the plume signals by 4.85–10.85 s, their cross-correlation coefficients peak (Figure 3a). Specifically, the highest cross-correlation coefficient of 0.91 emerges at 178.4 Hz with a time lag of 4.85 s. Such a significant lagging correlation can be visually recognized from the measured wave signals (Figures 3b and 3c). These observations support the spontaneous generation of hiss waves within the plasmaspheric plume and their subsequent propagation into the plasmaspheric core.

3. Modeling of Hiss Wave Generation and Migration

Based on the observation of RBSP-B at 17:41 UT on 12 February 2015, we use the previously developed code (Liu et al., 2018a, 2018b; Su et al., 2018a) to calculate the wave linear growth rate (C. Kennel, 1966; C. F. Kennel & Petschek, 1966; Chen et al., 2010) at the equator which is widely considered the wave source region in the inner magnetosphere (Chen et al., 2014; Church & Thorne, 1983; Thorne et al., 1973). There are mainly three inputs of this linear instability code: background magnetic field magnitude, cold electron density, and energetic electron phase space density at equator. We scale the observed magnetic field magnitude B_o to obtain the equatorial magnetic field magnitude $B_{eq} = B_o \cdot \overline{B}$ with the scaling factor $\overline{B}$ determined by the combined IGRF (Alken et al., 2021) and TS04 (Tsyganenko & Sitnov, 2005) model. Following the previous study (Denton et al., 2002), we scale the observed cold electron density N_e to obtain the equatorial cold electron density

$$N_{eq} = N_e \cos^{2\eta} \mathrm{MLAT}, \tag{1}$$

with the magnetic latitude MLAT and the latitudinal variation index $\eta = 2.5$ (Denton et al., 2002) for the specific calculation. Because the off-equatorial measurements do not allow us to determine the equatorial electron distribution near the pitch angle of 90°, we expediently use the local electron phase space density in the linear growth rate calculation. Considering that the growth of whistler-mode hiss waves is primarily driven by >10 keV electrons (Chen, Li, et al., 2012; Chen, Thorne, et al., 2012; Church & Thorne, 1983; Omura et al., 2015), we use the electron measurements from HOPE and RBSPICE at energy channels of 1.05–232.36 keV. In the overlapping energy range of HOPE and RBSPICE, we select the RBSPICE measurements with a higher pitch-angle resolution. To match the HOPE data at the high energy end, we scale up the RBSPICE data by a factor of 5 (Figure S1 in Supporting Information S1). For the HOPE data with significant fluctuations (Figure 4a), we

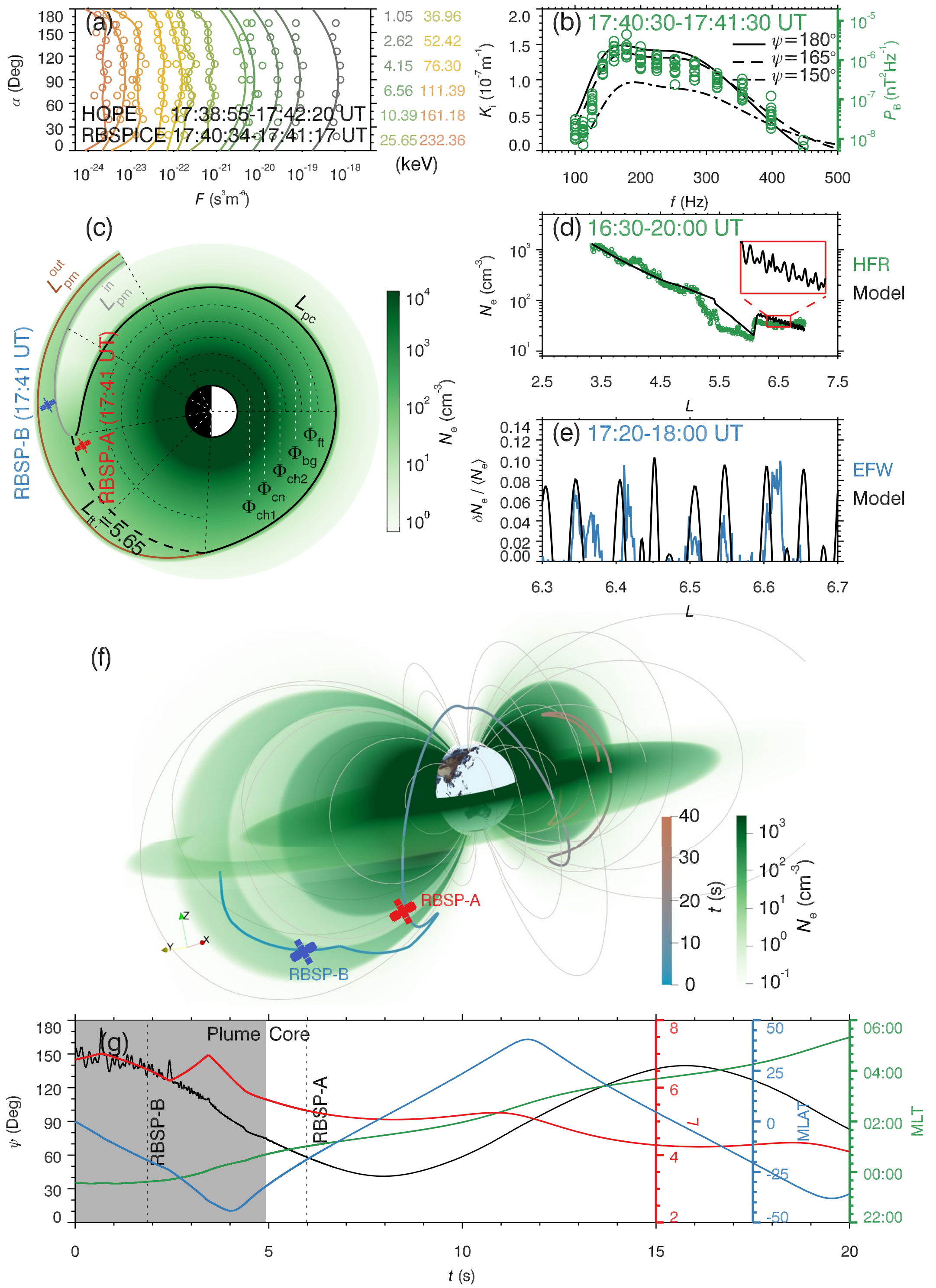

Figure 4.

approximate the electron pitch-angle distribution in the form of $F(E_k, \alpha) = F(E_k, \alpha = 90^\circ)\left(\frac{1+\sin\alpha}{2}\right)^{\sigma}$ at each energy channel, with the pitch angle index $\sigma = 2$. This approximation appears to overestimate the measured electron temperature anisotropy, more or less offsetting the underestimation bias of the equatorial anisotropy by the mid-latitude measurements. For the RBSPICE data (Figure 4a), we use a smooth cubic spline (Reinsch, 1967) to fit the electron pitch angle distribution at each energy channel. The linear theoretical model of the spontaneous instability of energetic electrons at the equator qualitatively explains the frequency-dependence of the observed wave intensities in the plume (Figure 4b). Specifically, both wave intensities and growth rates at normal angles of 150°–180° steeply increase from the low-frequency end, peak near 160 Hz, plateau within 200–280 Hz, and gradually decrease toward the high-frequency end. However, given the limited linear gain, additional nonlinear amplification (Omura et al., 2015) could be involved for waves to reach the observable level.

We use the ray-tracing code developed by Kimura (1966) to understand the propagation of hiss waves. For the simulation period without both storm and substorm activities in the inner magnetosphere ($L < 7$), we approximate the background magnetic field as a pure dipole. On the basis of the available density observations and the global PTP modeling results (Figures 1 and 2), we have constructed an analytical model of the cold electron density distribution

$$N_{\mathrm{e}}(L,\ \Phi,\ \mathrm{MLAT}) = N_{\mathrm{eq}}(L,\ \Phi)\cos^{-2\eta}\mathrm{MLAT}, \tag{2}$$

where N_{eq} is the equatorial density depending on magnetic shell L and longitude $\Phi = \frac{\mathrm{MLT}-12}{12}\pi$. The equatorial plasmaspheric outline (Figure 4c) consists of the boundary of the plasmaspheric core

$$L_{\mathrm{pc}} = \begin{cases} L_{\mathrm{p0}} & 0 \le \Phi < \Phi_{\mathrm{cn}}, \\ L_{\mathrm{ft}} - 0.1 - \left(L_{\mathrm{ft}} - 0.1 - L_{\mathrm{p0}}\right)\sqrt{1 - \dfrac{(\Phi - \Phi_{\mathrm{cn}})^2}{(\Phi_{\mathrm{ch2}} - \Phi_{\mathrm{cn}})^2}} & \Phi_{\mathrm{cn}} \le \Phi < \Phi_{\mathrm{ch2}}, \\ L_{\mathrm{p0}} + 1.7\mathrm{e}^{\frac{\left(\Phi - \Phi_{\mathrm{bg}}\right)^2}{\left(\Phi_{\mathrm{bg}} - \pi\right)^2}} & \Phi_{\mathrm{ft}} \le \Phi < 2\pi, \end{cases} \tag{3}$$

and the inner and outer boundaries of the plasmaspheric plume

$$L_{\mathrm{pm}}^{\mathrm{in}} = L_{\mathrm{ft}} + (8 - L_{\mathrm{ft}})\sqrt{1 - \frac{(\Phi + 1.39\pi)^2}{(\Phi_{\mathrm{ch2}} + 1.39\pi)^2}}, \tag{4}$$

$$L_{\mathrm{pm}}^{\mathrm{out}} = \begin{cases} 8.08\mathrm{e}^{-0.05\Phi} & \Phi_{\mathrm{ch1}} \le \Phi < \Phi_{\mathrm{bg}}, \\ L_{\mathrm{p0}} + 1.7\mathrm{e}^{\frac{\left(\Phi - \Phi_{\mathrm{bg}}\right)^2}{\left(\Phi_{\mathrm{bg}} - \pi\right)^2}} & \Phi_{\mathrm{bg}} \le \Phi < \Phi_{\mathrm{ft}}. \end{cases} \tag{5}$$

Here, $\Phi_{\mathrm{ch1}} = 0.67\pi$ and $\Phi_{\mathrm{ch2}} = 1.06\pi$ characterize the western and eastern termination of the channel between the plume and the core, $\Phi_{\mathrm{cn}} = 0.78\pi$ characterizes the transition between the trough and the channel, $\Phi_{\mathrm{bg}} = 1.25\pi$ characterizes the center of the bulge connected to the plume, $\Phi_{\mathrm{ft}} = 1.48\pi$ characterizes the eastern foot of the plume, $L_{\mathrm{ft}} = 5.65$ separates the plume's base from the core, and $L_{\mathrm{p0}} = 4.95$ is the duskside boundary of the core. The equatorial density is assumed to be

$$N_{\mathrm{eq}}(L,\ \Phi) = N_0(L) \cdot \overline{N_{\mathrm{fl}}(L,\ \Phi)} \cdot \overline{N_{\mathrm{tr}}(L,\ \Phi)} \cdot \overline{N_{\mathrm{ch}}(L,\ \Phi)}. \tag{6}$$

Figure 4. Modeling of the generation and propagation of waves. (a) Modeled (lines) and observed (circles) electron phase space density around 17:41 UT. (b) Frequency-dependence of the whistler-mode wave linear growth rates at different normal angles (black lines), in comparison with that of the wave magnetic power spectral densities (green circles) during 17:40:30–17:41:30 UT. (c) Modeled equatorial densities scaled by the magnitude of green saturation, the plasmaspheric outline (lines), and the mapped Radiation Belt Storm Probes (RBSP) locations at 17:41 UT (symbols). (d) Comparison between modeled (line) and observed (circles) densities along the RBSP-B orbit. The density fluctuation is visible in magnified view of modeled density profile. (e) Comparison between modeled (black) and observed (blue) density fluctuations in the plasmaspheric plume. By fitting the low-resolution HFR density data, the high-resolution density is calculated from the spacecraft potential measured by EFW: $N_{\mathrm{e}} = A_1\mathrm{e}^{A_3U} + A_2\mathrm{e}^{A_4U}$ with $A_1 = 90.73\ \mathrm{cm}^{-3}$, $A_2 = 43.11\ \mathrm{cm}^{-3}$, $A_3 = 0.55\ \mathrm{V}^{-1}$, and $A_4 = 0.30\ \mathrm{V}^{-1}$. (f) Three-dimensional path of the 178.4 Hz ray from the plume to the core within 40 s. The axis indicator of the geomagnetic coordinate system reflects the orientation of the current view. The ray path is color-coded according to time, and the background electron densities in the equatorial and meridional planes are scaled by the magnitude of green saturation. The gray lines represent the dipolar magnetic field lines rooted in the Earth. The two cartoon satellites indicate the positions of RBSP-B (blue) and RBSP-A (red) at 17:41 UT. (g) Temporal evolution of the normal angle (black), magnetic shell (red), magnetic latitude (blue), and magnetic local time (green) of the 178.4 Hz ray within 20 s.

where N_0 is a high-density basis, $\overline{N_{\mathrm{fl}}}$, $\overline{N_{\mathrm{tr}}}$, and $\overline{N_{\mathrm{ch}}}$ are three scaling factors to help create the density fluctuations of the plasmaspheric plume, the trough outside the plasmaspheric core, and the channel between plume and core, respectively. Following the early models (Chappell, 1974; Moldwin et al., 1994; Sheeley et al., 2001), we specify the density basis as

$$N_0 = C_0\left(\frac{C_1}{L}\right)^{C_2}, \tag{7}$$

with $C_0 = 125\ \mathrm{cm}^{-3}$, $C_1 = 5$, and $C_2 = 5.5$ based on the observations of RBSP-A and RBSP-B (Figure 4d). We set the density fluctuation factor in an ad-hoc way

$$\overline{N_{\mathrm{fl}}} = \begin{cases} [1 + S_{\mathrm{fl}}\cos(40\pi L)]\,[1 + S_{\mathrm{fl}}\cos(800\Phi)] & \Phi_{\mathrm{ch1}} < \Phi < \Phi_{\mathrm{ft}}, \\ 1 & \text{otherwise}, \end{cases} \tag{8}$$

with

$$S_{\mathrm{fl}} = 0.05\mathrm{e}^{\frac{-(L-L_{\mathrm{mid}})^6}{\Delta L^6}} \tag{9}$$

characterizing the fluctuation amplitude and

$$L_{\mathrm{mid}} = \begin{cases} 0.5\left(L_{\mathrm{pm}}^{\mathrm{in}} + L_{\mathrm{pm}}^{\mathrm{out}}\right) & \Phi_{\mathrm{ch1}} < \Phi \le \Phi_{\mathrm{ch2}}, \\ 0.5\left(L_{\mathrm{ft}} + L_{\mathrm{pm}}^{\mathrm{out}}\right) & \Phi_{\mathrm{ch2}} < \Phi \le \Phi_{\mathrm{ft}}, \end{cases} \tag{10}$$

and

$$\Delta L = \begin{cases} 0.5\left(L_{\mathrm{pm}}^{\mathrm{in}} - L_{\mathrm{pm}}^{\mathrm{out}}\right) & \Phi_{\mathrm{ch1}} < \Phi \le \Phi_{\mathrm{ch2}}, \\ 0.5\left(L_{\mathrm{pm}}^{\mathrm{out}} - L_{\mathrm{ft}}\right) & \Phi_{\mathrm{ch2}} < \Phi \le \Phi_{\mathrm{ft}}. \end{cases} \tag{11}$$

characterizing the radial coverage of fluctuations. The modeled lumps are distributed in checkerboard configuration. They have a peak amplitude of $\sim 0.1N_e$ and are spaced by ~ 0.05 in L, comparable to the observations by RBSP-B (Figure 4e). We set the trough factor as

$$\overline{N_{\mathrm{tr}}} = \begin{cases} (0.5 - 0.5R_{\mathrm{tr}})\cos\left[\dfrac{\pi\,(L - L_{\mathrm{tr}})}{W_{\mathrm{p}}}\right] + 0.5 + 0.5R_{\mathrm{tr}} & L_{\mathrm{tr}} < L \le L_{\mathrm{tr}} + W_{\mathrm{p}}, \\ R_{\mathrm{tr}} & L > L_{\mathrm{tr}} + W_{\mathrm{p}}, \\ 1 & \text{otherwise}, \end{cases} \tag{12}$$

with the boundary location

$$L_{\mathrm{tr}} = \begin{cases} L_{\mathrm{pm}}^{\mathrm{out}} & \Phi_{\mathrm{ch1}} < \Phi \le \Phi_{\mathrm{ft}}, \\ L_{\mathrm{pc}} & \text{otherwise}, \end{cases} \tag{13}$$

the transition width $W_{\mathrm{p}} = 0.2$, and the density ratio between trough and plasmasphere $R_{\mathrm{tr}} = 0.04$. We set the channel factor as

$$
\overline{N_{\mathrm{ch}}} = \begin{cases} (0.5 - 0.5R_{\mathrm{ch}})\cos\left[\dfrac{\pi\left(L_{\mathrm{pm}}^{\mathrm{in}} - L\right)}{W_{\mathrm{ch}}}\right] + 0.5 + 0.5R_{\mathrm{ch}} & \Phi_{\mathrm{ch1}} < \Phi < \Phi_{\mathrm{ch2}} \\ & L_{\mathrm{pm}}^{\mathrm{in}} - W_{\mathrm{ch}} < L < L_{\mathrm{pm}}^{\mathrm{in}}, \\ R_{\mathrm{ch}} & \Phi_{\mathrm{ch1}} < \Phi < \Phi_{\mathrm{ch2}} \\ & L_{\mathrm{pc}} + W_{\mathrm{ch}} < L \le L_{\mathrm{pm}}^{\mathrm{in}} - W_{\mathrm{ch}}, \\ (0.5 - 0.5R_{\mathrm{ch}})\cos\left[\dfrac{\pi\left(L - L_{\mathrm{pc}}\right)}{W_{\mathrm{ch}}}\right] + 0.5 + 0.5R_{\mathrm{ch}} & \Phi_{\mathrm{ch1}} < \Phi < \Phi_{\mathrm{ch2}} \\ & L_{\mathrm{pc}} < L \le L_{\mathrm{pc}} + W_{\mathrm{ch}}, \\ 1 & \text{otherwise}, \end{cases} \tag{14}
$$

where W_{ch} is the width of the transition layer

$$
W_{\mathrm{ch}} = \begin{cases} \dfrac{\Phi - \Phi_{\mathrm{cn}}}{\Phi_{\mathrm{ch2}} - \Phi_{\mathrm{cn}}}(W_{\mathrm{ch2}} - W_{\mathrm{ch1}}) + W_{\mathrm{ch1}} & \Phi_{\mathrm{cn}} < \Phi \le \Phi_{\mathrm{ch2}}, \\ W_{\mathrm{ch1}} & \Phi_{\mathrm{ch1}} < \Phi \le \Phi_{\mathrm{cn}}, \end{cases} \tag{15}
$$

with $W_{\mathrm{ch1}} = 0.2$ and $W_{\mathrm{ch2}} = 0.04$, and R_{ch} is the density ratio between the channel and plasmasphere

$$
R_{\mathrm{ch}} = \begin{cases} 10^{-\frac{\Phi - \Phi_{\mathrm{cn}}}{\Phi_{\mathrm{ch2}} - \Phi_{\mathrm{cn}}}\log_{10} R_{\mathrm{tr}} + \log_{10} R_{\mathrm{tr}}} & \Phi_{\mathrm{cn}} < \Phi \le \Phi_{\mathrm{ch2}}, \\ R_{\mathrm{tr}} & \Phi_{\mathrm{ch1}} < \Phi \le \Phi_{\mathrm{cn}}. \end{cases} \tag{16}
$$

Our analytical model has well reproduced the large-scale plasmaspheric core, channel and plume structures and qualitatively included the small-scale lumps embedded within the plasmaspheric plume (Figures 4d and 4e). Because the rays propagate far beyond the upper atmosphere, the electron density enhancement near the upper atmosphere is not taken into account.

We launch rays of 178.4 Hz from RBSP-B at the normal angles $\psi \in [120°, 180°]$ with 1° spacing and at the azimuthal angles $\varphi \in [0°, 360°]$ with 1.5° spacing. Note that the azimuthal angle is defined in the plane perpendicular to the magnetic field, with 0° and 90° for the projected wavevectors pointing anti-earthward and eastward directions, respectively. We record the rays that can reach the locations less than 0.2 R_{E} away from RBSP-A. By backward tracing from RBSP-B toward the equator, we can determine the equatorial source locations and angles of the rays that are able to propagate from RBSP-B to RBSP-A (Figure S2 in Supporting Information S1). Figures 4f and 4g present the results for a representative ray with the equatorial $\psi = 154.6°$ and $\varphi = 49.1°$ in the plasmaspheric plume. Because of the large-scale density enhancement of the plume and the small-scale density fluctuation embedded within the plume, this ray winds to RBSP-B at 1.86 s with its normal angle changed to 135°. In the subsequent 4.12 s, this ray refracts into the plasmaspheric core and propagates equatorward to RBSP-A with a normal angle of 58°. Therefore, our model effectively explains the wave propagation directions and timings deduced from the data (Figures 2 and 3). The hiss waves will disperse once they propagate into the plasmaspheric core with a larger volume. As a result, the hiss intensity decreased by approximately one order of magnitude from the plume to the core (Figures 2e and 2j). Inside the plasmaspheric core, hiss waves typically experience little Landau damping (Bortnik et al., 2008, 2011; Chen et al., 2009; Liu et al., 2020) and could spread over a broad range of L and MLT (Figures 4f and 4g). During the course of propagation, the repeated magnetospheric reflections could eventually disorder the Poynting flux directions of the hiss wave band.

4. Conclusion and Discussion

On the basis of data from three ground and space missions and detailed numerical modeling, we show that the plasmaspheric plume can act as an "engine" for the global plasmaspheric hiss, not only facilitating the local conversion of energy from energetic electrons to waves but also supplying waves to the plasmaspheric core.

Following a strong substorm, the GPS, THEMIS, and RBSP missions observed the rotating plasmaspheric plume on the dayside, duskside, and nightside, respectively. The hiss waves inside the plasmaspheric plume and core were observed by the RBSP mission to have opposite Poynting fluxes and highly correlate with each other at a time lag of 4.85–10.85 s. Furthermore, our linear instability calculations and ray-tracing simulations explain the frequency-dependence and propagation direction and timing of hiss waves inside the plasmaspheric plume and core.

Although we have made detailed observations for only a nightside residual plasmaspheric plume associated with a substorm, this depiction of the plume's role could be generalized over a broad spatiotemporal context. The plasmaspheric plume forms on the dayside in response to the enhanced magnetospheric convection during both substorms and storms and sweeps across all local times before disappearing (Borovsky & Denton, 2008; Darrouzet et al., 2009; Goldstein et al., 2004). As the plumes gradually become narrow and tenuous during the rotation, they are observed more frequently in the afternoon-dusk sector than in the other MLTs (Chappell, 1974; Goldstein et al., 2004; Kim & Shprits, 2019; Lee et al., 2016; Moldwin et al., 2004; Shi et al., 2019). Stronger magnetospheric convection would impel energetic electrons closer to Earth but erode the plasmasphere more deeply. Compared to the plasmaspheric core, the plasmaspheric plume extending outward is more accessible for energetic electrons and thus more favorable for wave growth (Kim & Shprits, 2019; Shi et al., 2019; Su et al., 2018a; Zhang et al., 2019). Other than the seemly structureless hiss waves reported here, whistler-mode waves with rising tones lasting ∼1 s also exist in the plasmaspheric plume (Shi et al., 2019; Woodroffe et al., 2017; Yu et al., 2018). Probably because of the eastward drift of energetic electrons, the plume whistler waves (Shi et al., 2019) statistically have higher amplitudes in the night-dawn-noon sector (on the order of 100 pT) than in the dusk sector (on the order of 50 pT) following strong substorms. With intense electron injections, the afternoon-dusk plumes have been reported to sustain the large-amplitude (up to 1.5 nT) whistler waves (Su et al., 2018a). Moreover, the plasmaspheric plume consisting of cold plasma lumps of enhanced density can guide both the structureless and structured whistler waves into the plasmaspheric core and allow these waves to evolve into the plasmaspheric hiss after mixing (Bortnik et al., 2008; Bortnik, Li, et al., 2009). Analogously, other plasmaspheric structures (Darrouzet et al., 2009) extending outward such as the plasmaspheric bulge, fingers, and crenulations could also become engines for plasmaspheric hiss (Tsurutani et al., 2015).

Acknowledgments
We acknowledge the WDC for Geomagnetism (Kyoto) and CDAWeb for the use of the AE and SYM-H indices; the International Global Navigation Satellite System Service (IGS) Ionosphere Working Group for the use of GPS-TEC data; K. H. Glassmeier, U. Auster, W. Baumjohann, R. E. Ergun, V. Angelopoulos, J. W. Bonnell, F. S. Mozer, C. W. Carlson, and J. P. McFadden for the use of FGM, DFB, EFI and ESA data of the THEMIS mission; C. A. Kletzing, W. S. Kurth, G. B. Hospodarsky, J. R. Wygant, H. E. Spence, G. D. Reeves, H. Funsten, and L. Lanzerotti for the use of EMFISIS, EFW, HOPE and RBSPICE data of the RBSP mission; and I. Kimura for the use of ray-tracing code. This work was supported by the Strategic Priority Research Program of Chinese Academy of Sciences (Grant no. XDB 41000000), the National Natural Science Foundation of China (Grant nos. 42188101, 42004140, and 42130204), the Chinese Academy of Sciences (Grant no. KZCX2-EW-QN510 and KZZD-EW-01-4), the CAS Key Research Program of Frontier Sciences (Grant no. QYZDB-SSW-DQC015), and the Key Research Program of the Chinese Academy of Sciences (Grant no. ZDRE-KT-2021-3).

Data Availability Statement

Van Allen Probes data are available at https://spdf.gsfc.nasa.gov/pub/data/rbsp/. THEMIS data are available at http://themis.ssl.berkeley.edu/data/themis/. GPS TEC maps are available at https://cdaweb.gsfc.nasa.gov/pub/data/. SYM-H, AE and Kp data are available at http://wdc.kugi.kyoto-u.ac.jp/wdc/Sec3.html. Ray-tracing code is available at http://waves.is.t.kanazawa-u.ac.jp/. The Plasmapause Test Particle simulation data is available at https://enarc.space.swri.edu/PTP/ or https://rbsp-ect.newmexicoconsortium.org/.

References

Alken, P., Thébault, E., Beggan, C. D., Amit, H., Aubert, J., Baerenzung, J., et al. (2021). International geomagnetic reference field: The thirteenth generation. *Earth Planets and Space*, *73*(1), 49. https://doi.org/10.1186/s40623-020-01288-x

Angelopoulos, V. (2008). The THEMIS mission. *Space Science Reviews*, *141*(1–4), 5–34. https://doi.org/10.1007/s11214-008-9336-1

Bonnell, J. W., Mozer, F. S., Delory, G. T., Hull, A. J., Ergun, R. E., Cully, C. M., et al. (2008). The electric field instrument (EFI) for THEMIS. *Space Science Reviews*, *141*(1–4), 303–341. https://doi.org/10.1007/s11214-008-9469-2

Borovsky, J. E., & Denton, M. H. (2008). A statistical look at plasmaspheric drainage plumes. *Journal of Geophysical Research*, *113*(A9), A09221. https://doi.org/10.1029/2007JA012994

Borovsky, J. E., & Valdivia, J. A. (2018). The Earth's magnetosphere: A systems science overview and assessment. *Surveys in Geophysics*, *39*(5), 817–859. https://doi.org/10.1007/s10712-018-9487-x

Bortnik, J., Chen, L., Li, W., Thorne, R. M., & Horne, R. B. (2011). Modeling the evolution of chorus waves into plasmaspheric hiss. *Journal of Geophysical Research*, *116*(A8), 8221. https://doi.org/10.1029/2011JA016499

Bortnik, J., Li, W., Thorne, R. M., Angelopoulos, V., Cully, C., Bonnell, J., et al. (2009). An observation linking the origin of plasmaspheric hiss to discrete chorus emissions. *Science*, *324*(5928), 775–778. https://doi.org/10.1126/science.1171273

Bortnik, J., Thorne, R. M., & Meredith, N. P. (2008). The unexpected origin of plasmaspheric hiss from discrete chorus emissions. *Nature*, *452*(7183), 62–66. https://doi.org/10.1038/nature06741

Bortnik, J., Thorne, R. M., & Meredith, N. P. (2009). Plasmaspheric hiss overview and relation to chorus. *Journal of Atmospheric and Solar-Terrestrial Physics*, *71*(16), 1636–1646. https://doi.org/10.1016/j.jastp.2009.03.023

Breneman, A. W., Halford, A., Millan, R., McCarthy, M., Fennell, J., Sample, J., et al. (2015). Global-scale coherence modulation of radiation-belt electron loss from plasmaspheric hiss. *Nature*, *523*(7559), 193–195. https://doi.org/10.1038/nature14515

Chan, K.-W., Holzer, R. E., & Smith, E. J. (1974). A relation between ELF hiss amplitude and plasma density in the outer plasmasphere. *Journal of Geophysical Research*, *79*(13), 1989–1993. https://doi.org/10.1029/JA079i013p01989

Chappell, C. R. (1974). Detached plasma regions in the magnetosphere. *Journal of Geophysical Research*, *79*(13), 1861–1870. https://doi.org/10.1029/JA079i013p01861

Chen, L., Bortnik, J., Li, W., Thorne, R. M., & Horne, R. B. (2012). Modeling the properties of plasmaspheric hiss: 1. Dependence on chorus wave emission. *Journal of Geophysical Research*, *117*(A5), 5201. https://doi.org/10.1029/2011JA017201

Chen, L., Bortnik, J., Thorne, R. M., Horne, R. B., & Jordanova, V. K. (2009). Three-dimensional ray tracing of VLF waves in a magnetospheric environment containing a plasmaspheric plume. *Geophysical Research Letters*, *36*(22), 22101. https://doi.org/10.1029/2009GL040451

Chen, L., Li, W., Bortnik, J., & Thorne, R. M. (2012). Amplification of whistler-mode hiss inside the plasmasphere. *Geophysical Research Letters*, *39*(8), 8111. https://doi.org/10.1029/2012GL051488

Chen, L., Thorne, R. M., Bortnik, J., Li, W., Horne, R. B., Reeves, G. D., et al. (2014). Generation of unusually low frequency plasmaspheric hiss. *Geophysical Research Letters*, *41*(16), 5702–5709. https://doi.org/10.1002/2014GL060628

Chen, L., Thorne, R. M., Jordanova, V. K., Wang, C.-P., Gkioulidou, M., Lyons, L., & Horne, R. B. (2010). Global simulation of EMIC wave excitation during the 21 April 2001 storm from coupled RCM-RAM-HOTRAY modeling. *Journal of Geophysical Research*, *115*(A7), 7209. https://doi.org/10.1029/2009JA015075

Chen, L., Thorne, R. M., Li, W., Bortnik, J., Turner, D., & Angelopoulos, V. (2012). Modulation of plasmaspheric hiss intensity by thermal plasma density structure. *Geophysical Research Letters*, *39*(14), 14103. https://doi.org/10.1029/2012GL052308

Church, S. R., & Thorne, R. M. (1983). On the origin of plasmaspheric hiss—Ray path integrated amplification. *Journal of Geophysical Research*, *88*(A10), 7941–7957. https://doi.org/10.1029/JA088iA10p07941

Darrouzet, F., Gallagher, D. L., André, N., Carpenter, D. L., Dandouras, I., Décréau, P. M. E., et al. (2009). Plasmaspheric density structures and dynamics: Properties observed by the CLUSTER and IMAGE missions. *Space Science Reviews*, *145*(1–2), 55–106. https://doi.org/10.1007/s11214-008-9438-9

Denton, R. E., Goldstein, J., & Menietti, J. D. (2002). Field line dependence of magnetospheric electron density. *Geophysical Research Letters*, *29*(24), 2205–2258. https://doi.org/10.1029/2002GL015963

Dunckel, N., & Helliwell, R. A. (1969). Whistler-mode emissions on the OGO 1 satellite. *Journal of Geophysical Research*, *74*(26), 6371–6385. https://doi.org/10.1029/JA074i026p06371

Foster, J. C., Coster, A. J., Erickson, P. J., Rich, F. J., & Sandel, B. R. (2004). Stormtime observations of the flux of plasmaspheric ions to the dayside cusp/magnetopause. *Geophysical Research Letters*, *31*(8), L08809. https://doi.org/10.1029/2004GL020082

Foster, J. C., Erickson, P. J., Coster, A. J., Goldstein, J., & Rich, F. J. (2002). Ionospheric signatures of plasmaspheric tails. *Geophysical Research Letters*, *29*(13), 1623. https://doi.org/10.1029/2002GL015067

Funsten, H. O., Skoug, R. M., Guthrie, A. A., MacDonald, E. A., Baldonado, J. R., Harper, R. W., et al. (2013). Helium, Oxygen, Proton, and Electron (HOPE) mass spectrometer for the Radiation Belt Storm Probes Mission. *Space Science Reviews*, *179*(1–4), 423–484. https://doi.org/10.1007/s11214-013-9968-7

Goldstein, J., Sandel, B. R., Thomsen, M. F., Spasojević, M., & Reiff, P. H. (2004). Simultaneous remote sensing and in situ observations of plasmaspheric drainage plumes. *Journal of Geophysical Research*, *109*(A3), 3202. https://doi.org/10.1029/2003JA010281

Goldstein, J., Thomsen, M. F., & DeJong, A. (2014). In situ signatures of residual plasmaspheric plumes: Observations and simulation. *Journal of Geophysical Research*, *119*(6), 4706–4722. https://doi.org/10.1002/2014JA019953

Green, J. L., Boardsen, S., Garcia, L., Taylor, W. W. L., Fung, S. F., & Reinisch, B. W. (2005). On the origin of whistler mode radiation in the plasmasphere. *Journal of Geophysical Research*, *110*(A3), A03201. https://doi.org/10.1029/2004JA010495

Hayakawa, M., Ohmi, N., Parrot, M., & Lefeuvre, F. (1986). Direction finding of elf hiss emissions in a detached plasma region of the magnetosphere. *Journal of Geophysical Research*, *91*(A1), 135–141. https://doi.org/10.1029/ja091ia01p00135

He, Z., Chen, L., Liu, X., Zhu, H., Liu, S., Gao, Z., & Cao, Y. (2019). Local generation of high-frequency plasmaspheric hiss observed by Van Allen probes. *Geophysical Research Letters*, *46*(3), 1141–1148. https://doi.org/10.1029/2018GL081578

He, Z., Yu, J., Chen, L., Xia, Z., Wang, W., Li, K., & Cui, J. (2020). Statistical study on locally generated high-frequency plasmaspheric hiss and its effect on suprathermal electrons: Van Allen probes observation and quasi-linear simulation. *Journal of Geophysical Research: Space Physics*, *125*(10), e28526. https://doi.org/10.1029/2020JA028526

Horne, R. B., & Thorne, R. M. (1998). Potential waves for relativistic electron scattering and stochastic acceleration during magnetic storms. *Geophysical Research Letters*, *25*(15), 3011–3014. https://doi.org/10.1029/98GL01002

Kennel, C. (1966). Low-frequency whistler mode. *Physics of Fluids*, *9*(11), 2190–2202. https://doi.org/10.1063/1.1761588

Kennel, C. F., & Petschek, H. E. (1966). Limit on stably trapped particle fluxes. *Journal of Geophysical Research*, *71*, 1–28. https://doi.org/10.1029/JZ071i001p00001

Kim, K.-C., & Shprits, Y. (2019). Statistical analysis of hiss waves in plasmaspheric plumes using Van Allen probe observations. *Journal of Geophysical Research: Space Physics*, *124*(3), 1904–1915. https://doi.org/10.1029/2018JA026458

Kimura, I. (1966). Effects of ions on whistler-mode ray tracing. *Radio Science*, *1*(3), 269–284. https://doi.org/10.1002/rds196613269

Kletzing, C. A., Kurth, W. S., Acuna, M., MacDowall, R. J., Torbert, R. B., Averkamp, T., et al. (2013). The electric and magnetic field instrument suite and integrated science (EMFISIS) on RBSP. *Space Science Reviews*, *179*(1–4), 127–181. https://doi.org/10.1007/s11214-013-9993-6

Kurth, W. S., Pascuale, S. D., Faden, J. B., Kletzing, C. A., Hospodarsky, G. B., Thaller, S., & Wygant, J. R. (2014). Electron densities inferred from plasma wave spectra obtained by the waves instrument on van Allen probes. *Journal of Geophysical Research*, *120*(2), 904–914. https://doi.org/10.1002/2014JA020857

Laakso, H., Santolik, O., Horne, R., Kolmasová, I., Escoubet, P., Masson, A., & Taylor, M. (2015). Identifying the source region of plasmaspheric hiss. *Geophysical Research Letters*, *42*(9), 3141–3149. https://doi.org/10.1002/2015GL063755

Lee, S. H., Zhang, H., Zong, Q. G., Otto, A., Rème, H., & Liebert, E. (2016). A statistical study of plasmaspheric plumes and ionospheric outflows observed at the dayside magnetopause. *Journal of Geophysical Research: Space Physics*, *121*(1), 492–506. https://doi.org/10.1002/2015JA021540

Lemaire, J. F., & Gringauz, K. I. (1998). In J. F. Lemaire & K. I. Gringauz (Eds.), *The Earth's plasmasphere*. Cambridge University Press.

Li, W., Chen, L., Bortnik, J., Thorne, R. M., Angelopoulos, V., Kletzing, C. A., et al. (2015). First evidence for chorus at a large geocentric distance as a source of plasmaspheric hiss: Coordinated THEMIS and Van Allen Probes observation. *Geophysical Research Letters*, *42*(2), 241–248. https://doi.org/10.1002/2014GL062832

Li, W., Shprits, Y. Y., & Thorne, R. M. (2007). Dynamic evolution of energetic outer zone electrons due to wave-particle interactions during storms. *Journal of Geophysical Research: Space Physics*, *112*(A10), A10220. https://doi.org/10.1029/2007JA012368

Li, W., Thorne, R. M., Bortnik, J., Reeves, G. D., Kletzing, C. A., Kurth, W. S., et al. (2013). An unusual enhancement of low-frequency plasmaspheric hiss in the outer plasmasphere associated with substorm-injected electrons. *Geophysical Research Letters*, *40*(15), 3798–3803. https://doi.org/10.1002/grl.50787

Liu, N., Su, Z., Gao, Z., Zheng, H., Wang, Y., Wang, S., et al. (2020). Comprehensive observations of substorm-enhanced plasmaspheric hiss generation, propagation, and dissipation. *Geophysical Research Letters*, *47*(2), e86040. https://doi.org/10.1029/2019GL086040

Liu, N., Su, Z., Zheng, H., Wang, Y., & Wang, S. (2018a). Magnetosonic harmonic falling and rising frequency emissions potentially generated by nonlinear wave-wave interactions in the Van Allen radiation belts. *Geophysical Research Letters*, *45*(16), 7985–7995. https://doi.org/10.1029/2018GL079232

Liu, N., Su, Z., Zheng, H., Wang, Y., & Wang, S. (2018b). Prompt disappearance and emergence of radiation belt magnetosonic waves induced by solar wind dynamic pressure variations. *Geophysical Research Letters*, *45*(2), 585–594. https://doi.org/10.1002/2017GL076382

Lyons, L. R., Thorne, R. M., & Kennel, C. F. (1972). Pitch-angle diffusion of radiation belt electrons within the plasmasphere. *Journal of Geophysical Research*, *77*(19), 3455–3474. https://doi.org/10.1029/JA077i019p03455

Mauk, B. H., Fox, N. J., Kanekal, S. G., Kessel, R. L., Sibeck, D. G., & Ukhorskiy, A. (2013). Science objectives and rationale for the radiation belt storm probes mission. *Space Science Reviews*, *179*(1–4), 3–27. https://doi.org/10.1007/s11214-012-9908-y

McFadden, J. P., Carlson, C. W., Larson, D., Ludlam, M., Abiad, R., Elliott, B., et al. (2008). The THEMIS ESA plasma instrument and in-flight calibration. *Space Science Reviews*, *141*(1–4), 277–302. https://doi.org/10.1007/s11214-008-9440-2

Meredith, N. P., Bortnik, J., Horne, R. B., Li, W., & Shen, X.-C. (2021). Statistical investigation of the frequency dependence of the chorus source mechanism of plasmaspheric hiss. *Geophysical Research Letters*, *48*(6), e92725. https://doi.org/10.1029/2021GL092725

Meredith, N. P., Horne, R. B., Bortnik, J., Thorne, R. M., Chen, L., Li, W., & Sicard-Piet, A. (2013). Global statistical evidence for chorus as the embryonic source of plasmaspheric hiss. *Geophysical Research Letters*, *40*(12), 2891–2896. https://doi.org/10.1002/grl.50593

Meredith, N. P., Horne, R. B., Glauert, S. A., & Anderson, R. R. (2007). Slot region electron loss timescales due to plasmaspheric hiss and lightning-generated whistlers. *Journal of Geophysical Research*, *112*(A8), 8214. https://doi.org/10.1029/2007JA012413

Moldwin, M. B., Howard, J., Sanny, J., Bocchicchio, J. D., Rassoul, H. K., & Anderson, R. R. (2004). Plasmaspheric plumes: CRRES observations of enhanced density beyond the plasmapause. *Journal of Geophysical Research*, *109*(A5), A05202. https://doi.org/10.1029/2003JA010320

Moldwin, M. B., Thomsen, M. F., Bame, S. J., McComas, D. J., & Moore, K. R. (1994). An examination of the structure and dynamics of the outer plasmasphere using multiple geosynchronous satellites. *Journal of Geophysical Research*, *99*(A6), 11475–11482. https://doi.org/10.1029/93JA03526

Nakamura, S., Omura, Y., & Summers, D. (2018). Fine structure of whistler mode hiss in plasmaspheric plumes observed by the Van Allen probes. *Journal of Geophysical Research: Space Physics*, *123*(11), 9055–9064. https://doi.org/10.1029/2018JA025803

Nakamura, S., Omura, Y., Summers, D., & Kletzing, C. A. (2016). Observational evidence of the nonlinear wave growth theory of plasmaspheric HISS. *Geophysical Research Letters*, *43*(19), 10040–10049. https://doi.org/10.1002/2016GL070333

Ni, B., Li, W., Thorne, R. M., Bortnik, J., Ma, Q., Chen, L., et al. (2014). Resonant scattering of energetic electrons by unusual low-frequency hiss. *Geophysical Research Letters*, *41*(6), 1854–1861. https://doi.org/10.1002/2014GL059389

Nishimura, Y., Goldstein, J., Martinis, C., Ma, Q., Li, W., Zhang, S. R., et al. (2022). Multi-scale density structures in the plasmaspheric plume during a geomagnetic storm. *Journal of Geophysical Research: Space Physics*, *127*(3), e30230. https://doi.org/10.1029/2021JA030230

Omura, Y., Nakamura, S., Kletzing, C. A., Summers, D., & Hikishima, M. (2015). Nonlinear wave growth theory of coherent hiss emissions in the plasmasphere. *Journal of Geophysical Research*, *120*(9), 7642–7657. https://doi.org/10.1002/2015JA021520

Reinsch, C. H. (1967). Smoothing by spline functions. *Numerische Mathematik*, *10*(3), 177–183. https://doi.org/10.1007/bf02162161

Russell, C. T., Holzer, R. E., & Smith, E. J. (1969). OGO 3 observations of ELF noise in the magnetosphere. 1. Spatial extent and frequency of occurrence. *Journal of Geophysical Research*, *74*, 755–777. https://doi.org/10.1029/JA074i003p00755

Santolík, O., Parrot, M., & Lefeuvre, F. (2003). Singular value decomposition methods for wave propagation analysis. *Radio Science*, *38*(1), 1010. https://doi.org/10.1029/2000RS002523

Santolík, O., Pickett, J. S., Gurnett, D. A., Menietti, J. D., Tsurutani, B. T., & Verkhoglyadova, O. (2010). Survey of Poynting flux of whistler mode chorus in the outer zone. *Journal of Geophysical Research*, *115*(A7), A00F13. https://doi.org/10.1029/2009JA014925

Santolík, O., Pickett, J. S., Gurnett, D. A., & Storey, L. R. O. (2002). Magnetic component of narrowband ion cyclotron waves in the auroral zone. *Journal of Geophysical Research*, *107*(A12), 1444. https://doi.org/10.1029/2001JA000146

Sheeley, B. W., Moldwin, M. B., Rassoul, H. K., & Anderson, R. R. (2001). An empirical plasmasphere and trough density model: Crres observations. *Journal of Geophysical Research*, *106*(A11), 25631–25642. https://doi.org/10.1029/2000JA000286

Shi, R., Li, W., Ma, Q., Green, A., Kletzing, C. A., Kurth, W. S., et al. (2019). Properties of whistler mode waves in Earth's plasmasphere and plumes. *Journal of Geophysical Research*, *124*(2), 1035–1051. https://doi.org/10.1029/2018JA026041

Sonwalkar, V. S., & Inan, U. S. (1989). Lightning as an embryonic source of VLF hiss. *Journal of Geophysical Research*, *94*(A6), 6986–6994. https://doi.org/10.1029/JA094iA06p06986

Spence, H. E., Reeves, G. D., Baker, D. N., Blake, J. B., Bolton, M., Bourdarie, S., et al. (2013). Science goals and overview of the Radiation belt storm probes (RBSP) Energetic particle, composition, and thermal plasma (ECT) suite on NASA's Van Allen probes mission. *Space Science Reviews*, *179*(1–4), 311–336. https://doi.org/10.1007/s11214-013-0007-5

Su, Z., Liu, N., Zheng, H., Wang, Y., & Wang, S. (2018a). Large-amplitude extremely low frequency hiss waves in plasmaspheric plumes. *Geophysical Research Letters*, *45*(2), 565–577. https://doi.org/10.1002/2017GL076754

Su, Z., Liu, N., Zheng, H., Wang, Y., & Wang, S. (2018b). Multipoint observations of nightside plasmaspheric hiss generated by substorm-injected electrons. *Geophysical Research Letters*, *45*(20), 10. https://doi.org/10.1029/2018GL079927

Su, Z., Xiao, F., Zheng, H., & Wang, S. (2011). CRRES observation and STEERB simulation of the 9 October 1990 electron radiation belt dropout event. *Geophysical Research Letters*, *38*(6), L06106. https://doi.org/10.1029/2011GL046873

Summers, D., Ni, B., Meredith, N. P., Horne, R. B., Thorne, R. M., Moldwin, M. B., & Anderson, R. R. (2008). Electron scattering by whistler-mode ELF hiss in plasmaspheric plumes. *Journal of Geophysical Research*, *113*(A4), A04219. https://doi.org/10.1029/2007JA012678

Summers, D., Omura, Y., Nakamura, S., & Kletzing, C. A. (2014). Fine structure of plasmaspheric hiss. *Journal of Geophysical Research: Space Physics*, *119*(11), 9134–9149. https://doi.org/10.1002/2014JA020437

Summers, D., Thorne, R. M., & Xiao, F. (1998). Relativistic theory of wave-particle resonant diffusion with application to electron acceleration in the magnetosphere. *Journal of Geophysical Research*, *103*(A9), 20487–20500. https://doi.org/10.1029/98JA01740

Thorne, R. M., Church, S. R., & Gorney, D. J. (1979). On the origin of plasmaspheric hiss - the importance of wave propagation and the plasmapause. *Journal of Geophysical Research*, *84*(A9), 5241–5247. https://doi.org/10.1029/JA084iA09p05241

Thorne, R. M., Li, W., Ni, B., Ma, Q., Bortnik, J., Chen, L., et al. (2013). Rapid local acceleration of relativistic radiation-belt electrons by magnetospheric chorus. *Nature*, *504*(7480), 411–414. https://doi.org/10.1038/nature12889

Thorne, R. M., Smith, E. J., Burton, R. K., & Holzer, R. E. (1973). Plasmaspheric hiss. *Journal of Geophysical Research*, *78*(10), 1581–1596. https://doi.org/10.1029/JA078i010p01581

Tsurutani, B. T., Falkowski, B. J., Pickett, J. S., Santolik, O., & Lakhina, G. S. (2015). Plasmaspheric hiss properties: Observations from polar. *Journal of Geophysical Research*, *120*(1), 414–431. https://doi.org/10.1002/2014JA020518

Tsurutani, B. T., Smith, E. J., & Thorne, R. M. (1975). Electromagnetic hiss and relativistic electron losses in the inner zone. *Journal of Geophysical Research*, *80*(4), 600–607. https://doi.org/10.1029/JA080i004p00600

Tsyganenko, N. A., & Sitnov, M. I. (2005). Modeling the dynamics of the inner magnetosphere during strong geomagnetic storms. *Journal of Geophysical Research*, *110*(A3), A03208. https://doi.org/10.1029/2004JA010798

Wang, C., Zong, Q., Xiao, F., Su, Z., Wang, Y., & Yue, C. (2011). The relations between magnetospheric chorus and hiss inside and outside the plasmasphere boundary layer: Cluster observation. *Journal of Geophysical Research*, *116*(A7), A07221. https://doi.org/10.1029/2010JA016240

Woodroffe, J. R., Jordanova, V. K., Funsten, H. O., Streltsov, A. V., Bengtson, M. T., Kletzing, C. A., et al. (2017). Van Allen Probes observations of structured whistler mode activity and coincident electron Landau acceleration inside a remnant plasmaspheric plume. *Journal of Geophysical Research: Space Physics*, *122*(3), 3073–3086. https://doi.org/10.1002/2015JA022219

Wygant, J., Bonnell, J., Goetz, K., Ergun, R., Mozer, F., Bale, S., et al. (2013). The electric field and waves instruments on the radiation belt storm probes mission. *Space Science Reviews*, *179*(1–4), 183–220. https://doi.org/10.1007/s11214-013-0013-7

Yu, J., Li, L. Y., Cui, J., & Wang, J. (2018). Ultrawideband rising-tone chorus waves observed inside the oscillating plasmapause. *Journal of Geophysical Research: Space Physics*, *123*(8), 6670–6678. https://doi.org/10.1029/2018JA025875

Zhang, W., Ni, B., Huang, H., Summers, D., Fu, S., Xiang, Z., et al. (2019). Statistical properties of hiss in plasmaspheric plumes and associated scattering losses of radiation belt electrons. *Geophysical Research Letters*, *46*(11), 5670–5680. https://doi.org/10.1029/2018GL081863